

Polytypism phenomenon in GaN nanocrystals grown on van der Waals surface

Y.E. Maidebura¹, V.G. Mansurov¹, T.V. Malin¹, I.A. Aleksandrov¹, K.S. Zhuravlev¹, B. Pecz²

¹Rzhanov Institute of Semiconductor Physics SB RAS, Novosibirsk, Russia

²Centre for Energy Research, Institute of Technical Physics and Materials Science, Konkoly-Thege ut 29-33, 1121 Budapest, Hungary

¹maid@isp.nsc.ru, ORCID: 0000-0001-6380-950X

ABSTRACT. The polytypism phenomenon in the growth of nanostructures reveals new properties and opportunities for bandgap engineering by enabling controlled formation of different phases of the same material with distinct crystalline and electronic structures. In the case of III-nitrides, the occurrence of polytypism is unlikely and has not been experimentally observed to date. Here, we report the discovery of polytypism in GaN nanocrystals (NCs) grown via the vapor-liquid-solid mechanism on the surface of a van der Waals graphene-like SiN structure. Through a detailed analysis of the diffraction patterns, we have established the formation of three structures during the growth of NCs, namely zinc-blende with the (111) plane, the 6H polytype and wurtzite with the non-polar (10-10) plane. As shown by transmission electron microscopy data, the crystal structures form within the volume of a single NC. The formation of zinc-blende and wurtzite phases is explained within the framework of classical nucleation theory, while the 6H polytype nucleates at the boundary between these phases. Calculations indicate the possibility of growing NCs with either pure zinc-blende or wurtzite structures. In essence, this study introduces new degree of freedom in the growth and application of GaN-based nanostructures grown via the vapor-liquid-solid method.

I. INTRODUCTION

Nanostructures, such as two-dimensional materials, quantum wells, wires and dots, have become some of the most advanced and promising objects in modern research in materials science and condensed matter physics. In nanostructures, new and remarkable phenomena have been discovered, such as the quantum Hall effect, conductance quantization, Coulomb blockade, topological effects, tunnel magnetoresistance, etc. Furthermore, the use of nanostructures has seen a marked increase the development of various optoelectronic and electronic devices¹, spintronic systems², biomedical applications^{3,4} and catalysis^{5,6}. Of particular interest are GaN-based nanostructures due to their unique properties, such as a wide bandgap, high exciton binding energy and oscillator strength, large effective mass of electrons and holes, and the presence of a high built-in electric field (with a strength of the order of MV/cm in wurtzite GaN). GaN-based nanostructures have already been demonstrated in HEMTs^{7,8}, LEDs and laser diodes^{9,10}, single-photon emitters^{11,12}, solar cells¹³, photodetectors^{14,15} and single-electron transistors^{16,17}. The breadth of both fundamental and applied research on nanostructures is driven by their unique properties and the potential for wide tunability due to their discrete electronic structure and high surface-to-volume ratio. Structural, optical, chemical, and electronic properties can be extensively modified depending on the size, shape and surface functionalization of the nanostructures.

New properties and methods of bandgap engineering in nanostructures are anticipated due to the phenomenon of polytypism¹⁸⁻²¹, which involves the formation of different phases of the same material with distinct crystalline and electronic structures within the volume of the nanostructure. Such polytype or crystal heterostructures offer significant advantages over conventional ones due to the absence of strain and atomically sharp interfaces. Polytype heterostructures have been synthesized and are the focus of active investigation in nanowires²²⁻²⁷ and 2D material systems²⁸⁻³⁰. The greatest success in the controlled formation of polytype heterostructures has been achieved in the growth of nanowires in III-V systems via the vapor-liquid-solid (VLS) mechanism. III-V semiconductors (e.g., GaAs, InAs), which typically adopt

the stable zinc blende (ZB) structure, can acquire the metastable wurtzite (WZ) structure when grown in nanowire form. Numerous studies have been conducted to explain and investigate the occurrence of polytypism in III-V nanowires^{31–36}. According to the current understanding outlined by Glas et al.³³, the formation of the WZ phase is triggered at the triple phase line, while the ZB phase forms away from it. The higher cohesive energy of the WZ phase is offset by the lower surface energy of the side facets of the nucleus³³. III-nitrides differ from other III-V materials due to their high bond ionicity, leading to the WZ structure as a stable one. Therefore, GaN grown on surfaces with random orientations, such as on amorphous Si_xN_y , typically adopts the WZ structure³⁷. The formation of GaN with either ZB or WZ structures can be promoted by selecting substrates with four-fold or six-fold symmetry, respectively^{38–41}. Based on studies of polytypism in III-V nanowires, polytypism in III-N nanostructures grown by the VLS method is considered to be unexpected^{42,43}. In the few studies reporting polytypism in GaN nanowires, it was associated with stacking faults in the form of ZB phase inclusions, which form during strain relaxation^{44,45} or under heavy Mg doping^{46,47}.

In this study, we report the phenomenon of polytypism in GaN nanocrystals (NCs) grown by the VLS method on a van der Waals surface of graphene-like SiN. Using transmission geometry in high-energy electron diffraction, we thoroughly investigated the structure and formation processes of the NCs. Combined with azimuthal dependence, we have identified the nature of all diffraction spots and established the formation of three structures during NCs growth, namely ZB with the (111) plane, the 6H polytype and WZ with the nonpolar (10-10) plane. As indicated by the data obtained from transmission electron microscopy, the formation of crystal structures is occurring within the volume of a single NC. By analyzing the kinetics of the main and fractional diffraction spots, which characterize the respective structures, it was established that the formation of crystal structures occurs simultaneously. The variety of phases within the NCs was explained within the framework of classical nucleation theory, where the nucleation of the ZB phase is

energetically favorable at the liquid/vapor/substrate triple phase line, while the nucleation of the WZ phase is favored away from this boundary.

II. METHODS

The investigation of the crystalline structure and formation processes of NCs on the surface of g-SiN was conducted *in situ* using a Riber CBE-32 molecular beam epitaxy (MBE) setup. Ammonia with a purity of 99.999999% was used as the nitrogen source, further purified with an Entegris mechanical filter to remove particles larger than 0.01 μm . The ammonia pressure in the growth chamber was controlled using a mass flow controller. A Knudsen effusion cell was used as the gallium source. The substrate temperature was measured using an Iacon pyrometer, a thermocouple, and an Ocean Optics USB4000 miniature spectrometer. The spectrometer enabled a temperature measurement method based on detecting the emission spectrum of the heated substrate, as described elsewhere⁴⁸. The accuracy of this method for determining the growth surface temperature is ± 5 °C, as detailed in⁴⁹. The Si (111) substrate was prepared using a modified Shiraki method and cleaned by annealing in the growth chamber at 1076 °C. The g-SiN layer was formed by exposing the substrate to an ammonia flow of 10 sccm at 960 °C for 6 seconds, as detailed in^{50,51}. The formation of the g-SiN layer was confirmed by the appearance of an 8×8 superstructure in the diffraction pattern. After forming the g-SiN layer, the temperature was lowered to 575 °C, 600 °C, or 625 °C, the ammonia flow was stopped, and Ga droplets were deposited for 30 seconds at a Ga flux of 0.1 monolayers per second. The droplets were then annealed in an ammonia flow of 250 sccm for 4.5 minutes. The study of NCs formation and structure was performed using reflection high-energy electron diffraction (RHEED). The evolution of the diffraction patterns was recorded and analyzed using a kSA400 system. The crystal structure of the NCs was investigated by means of high-resolution transmission electron microscopy (HRTEM) on a FEI THEMIS 200 system.

III. RESULTS

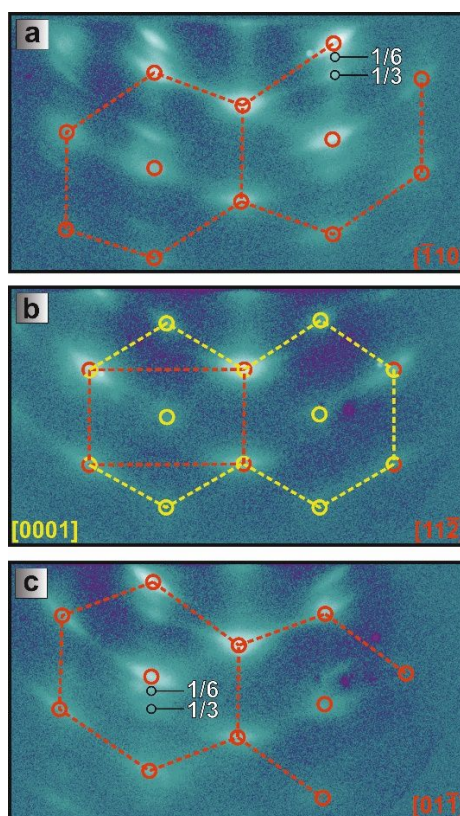


Figure 1. Diffraction patterns of GaN NCs at azimuthal angles of (a) 0° , (b) 30° and (c) 60° , respectively.

Red and yellow circles highlight the fundamental spots of GaN.

The diffraction patterns of GaN NCs at azimuthal angles of 0° , 30° and 60° are shown in Figure 1a, 1b and 1c, respectively. The rotation was performed around an axis perpendicular to the sample surface. Diffraction represents an ordered arrangement of spots, known as Bragg spots, that are concentrically blurred over a small angle. The arrangement of spots in transmission diffraction represents a cross-section of the reciprocal lattice by the Ewald sphere and provides information about the crystal structure of NCs⁵². In Figure 1a, the spots highlighted with red circles and connected with dashed red lines for clarity correspond to the fundamental GaN spots. To confirm the identification of these spots as fundamental ones, the intensity kinetics of the spots were measured, as shown below. Horizontally, only fundamental spots are observed in the diffraction pattern, while vertically, both fundamental and fractional $1/3$ and $1/6$ spots, which divide the distance between the fundamental spots by 3 and 6, are visible. As can be seen in Figure

1b, upon rotation by 30°, the fractional 1/3 and 1/6 spots disappear, and the diffraction pattern consists of two sets of fundamental spots forming a rectangle (red circles) and a regular hexagon (yellow circles). At an azimuthal angle of 60° (see Figure 1c), the fractional spots reappear, and the arrangement of the spots in the diffraction pattern corresponds to that at the 0° azimuthal angle.

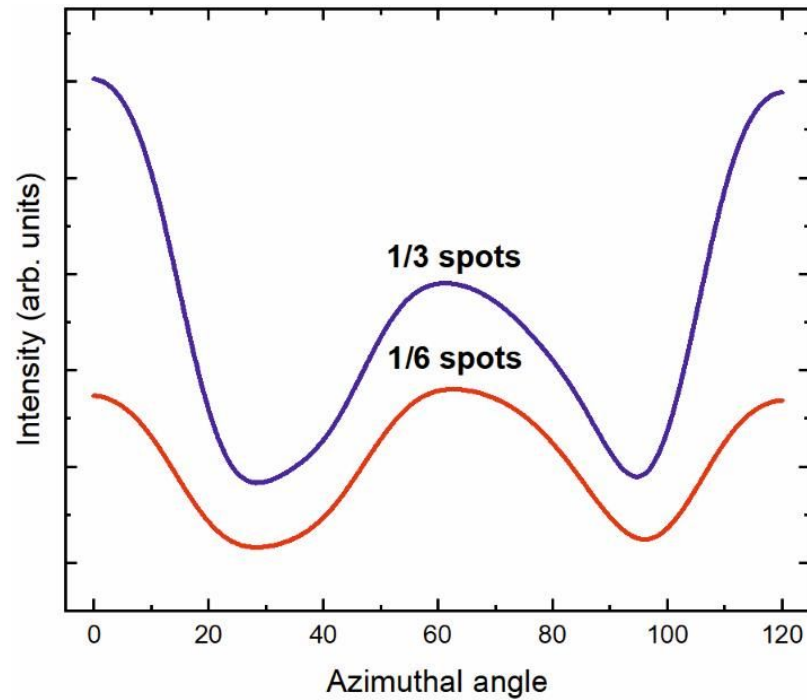


Figure 2. The intensity of 1/3 and 1/6 spots versus azimuthal angle.

To unambiguously determine the crystal structures associated with the 1/3 and 1/6 spots, the intensity dependencies of these spots on the azimuthal angle were measured. The symmetry of the spots intensity during rotation around a specific axis is determined by the rotational symmetry of the crystal structure relative to that axis. This follows from the scattering amplitude of the electron beam by atoms, which, in the direction of the reciprocal lattice vector, is determined by the structure factor:

$$F(hkl) = f_{Ga} \sum_n \exp(-2\pi i(hx_n + ky_n + lz_n)) + f_N \sum_m \exp(-2\pi i(hx_m + ky_m + lz_m)) \quad (1)$$

where f_{Ga} and f_N are the atomic scattering factors of Ga and N atoms, and $x_{n,m} + y_{n,m} + z_{n,m}$ are the coordinates that define the positions of the atoms within the unit cell. According to the equation (1), the rotational symmetry of the unit cell depends on the positions of the atoms and determines the azimuthal angle dependence of the spot intensity, which is directly proportional to the square of the scattering amplitude modulus. Figure 2 shows the intensity dependence of the 1/3 and 1/6 spots as a function of the azimuthal angle. The diffraction pattern with the maximum intensity for each respective spot is observed at zero degrees. As demonstrated in Figure 2, a 60° change in the azimuthal angle results in a decrease in the intensity of the 1/3 spot relative to its intensity at 0°. Conversely, at 120°, the intensity reverts to the value observed at 0°. The intensity of the 1/6 spot, on the other hand, remains unaltered when the azimuthal angle is rotated by either 60° or 120°.

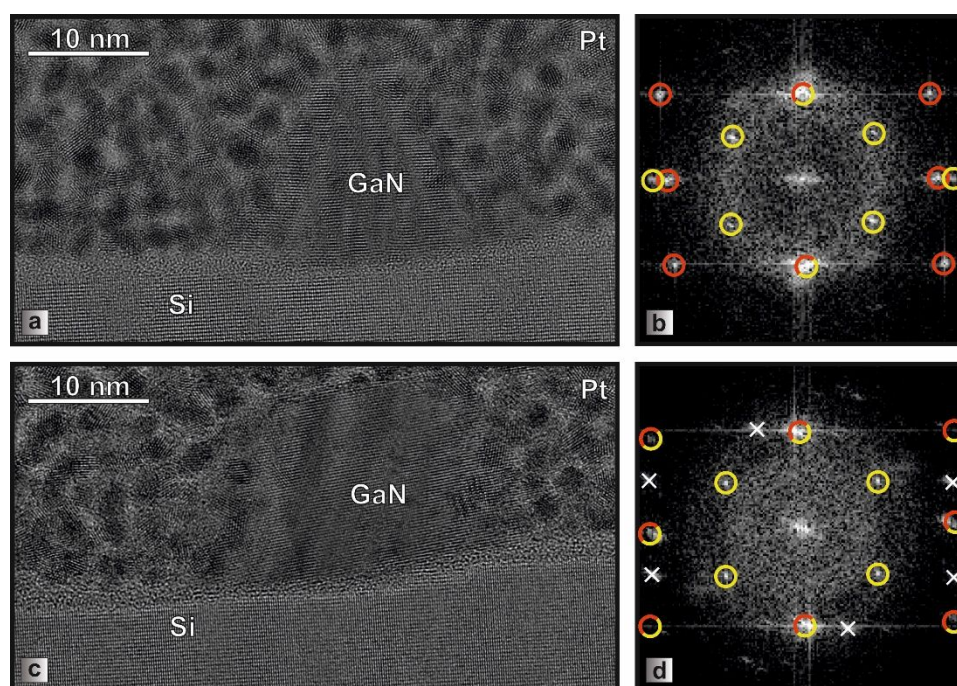


Figure 3. HRTEM images of GaN nanocrystals (a), (c) with corresponding FFT patterns (b), (d). Red and yellow circles highlight the fundamental spots of GaN, similarly as in Figure 1b, whereas the white crosses highlight spots from the Moiré pattern.

The diffraction patterns obtained by the RHEED method provide an integral representation of the crystal structure of NCs. To study the structure of individual NCs, HRTEM measurements

were performed with the use of fast Fourier transform (FFT). The plane of the investigated HRTEM images corresponds to the plane (11-2) of the Si substrate. Figure 3a and c illustrate HRTEM images of two NCs located on a thin layer of amorphous SiN (less than 0.5 nm thick). Outside the NC base, amorphous SiN with a thickness of approximately 2 nm is observed, which is attributed to the transformation of the g-SiN layer when it is exposed in an ammonia flow^{50,51,53}. Presumably, during NC formation, some of the ammonia is used to form amorphous SiN from g-SiN, although the g-SiN can be preserved not only during GaN NCs formation⁵⁴, but also during continuous AlN growth⁵⁵. The NCs possess a truncated pyramid shape with a wetting angle of approximately 60°, a height of about 16 nm, and base dimensions of ≈25 and 30 nm. As can be seen in Figures 3b and 3d, the FFT images of NCs are formed by the two sets of spots highlighted by the red and yellow circles, whereas the spots highlighted by the white crosses in Figure 3d are formed due to the Moiré pattern. It is worth noting that the arrangement of spots in the FFT images corresponds to that in the RHEED pattern at an azimuthal angle of 30° (see Figure 1b).

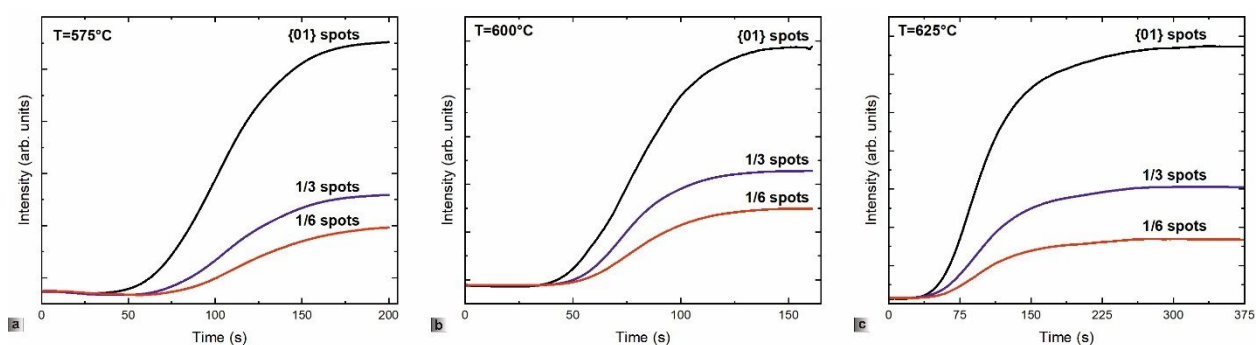


Figure 4. Intensity kinetics of {01}, 1/3 and 1/6 spots during exposure of gallium droplets in ammonia flow at temperatures of 575, 600 and 625 °C (a), (b) and (c), respectively.

Due to the formation of crystal structures with different rotational symmetries within the NCs, the intensity kinetics of both fundamental and fractional spots were measured at various points on the diffraction pattern and subsequently averaged. The fundamental GaN spots are referred to as {01} throughout the text. Figure 4a, 4b and 4c illustrates the intensity kinetics of the {01}, 1/3 and 1/6 spots, respectively, during the exposure of Ga droplets to an ammonia flow at temperatures of 575 °C, 600 °C and 625 °C. As can be seen from the figures, the {01} spots on

the diffraction pattern appear earlier than the $1/3$ and $1/6$ spots at $575\text{ }^{\circ}\text{C}$ and $600\text{ }^{\circ}\text{C}$, whereas at $625\text{ }^{\circ}\text{C}$, the spots emerge simultaneously. The appearance of spots on the diffraction pattern indicates the onset of constructive interference dominance of the electron beam at the NC structure, which surpasses the scattering of the electron beam in the gallium droplet. Given that crystal formation during VLS growth begins either at the liquid/solid interface or at the triple phase line, the earlier appearance of fundamental spots relative to fractional ones suggests the establishment of vertical periodicity in the NC with a period of a one interplanar distance. In contrast, structures with vertical periodicities of 3 and 6 interplanar distances, associated with the $1/3$ and $1/6$ spots, possess a smaller volume for fractional spot formation. Therefore, the intensity kinetics of the $1/3$ and $1/6$ spots at $575\text{ }^{\circ}\text{C}$ and $600\text{ }^{\circ}\text{C}$ are governed by the rate of formation of the corresponding structures. At $625\text{ }^{\circ}\text{C}$, the spot intensity kinetics slows down due to the evaporation of Ga droplets⁵⁴, and the simultaneous appearance of both fundamental and fractional spots. At $636\text{ }^{\circ}\text{C}$, NCs formation is not observed, presumably due to the extensive evaporation of Ga droplets⁵⁴.

IV. DISCUSSION

IVa. Identification of crystal structures

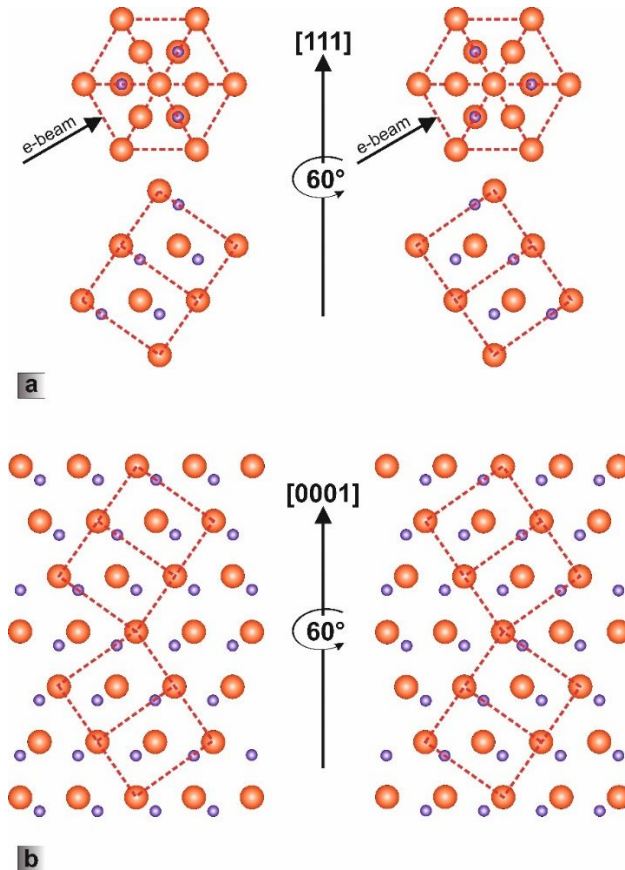


Figure 5. (a) ZB structure at an azimuthal angle of 0° (plane (111) above, plane (-1-10) below) and an azimuthal angle of 60° (plane (111) above, plane (01-1) below). The rotation is performed relative to the [111] axis. (b) Structure 6H at an azimuthal angle of 0° (plane (11-20)) and an azimuthal angle of 60° (plane (2-1-10)). The rotation is performed with respect to the [0001] axis. Red and violet spheres are gallium and nitrogen atoms, respectively. The red dashed lines indicate the unit cells of the ZB structure.

The appearance of fractional $1/3$ and $1/6$ spots on the RHEED patterns indicates the existence of two structures with periods of 3 and 6 interplanar spacings d in the growth direction. These structures exhibit three-fold and six-fold rotational symmetries, respectively. According to the literature, the structure with a period of $3d$ corresponds to the ZB structure with the (111) plane,

while the structure with a period of $6d$ corresponds to the 6H polytype, which forms at the boundary between the WZ and ZB structures^{54,56,57}. To explain the rotational symmetry of these structures, Figure 5 shows the unit cell of the ZB structure in the (111) and $\{-110\}$ planes, and the 6H structure in the $\{11-20\}$ planes. The ZB and 6H structures are rotated by 0° and 60° around the [111] and [0001] axes, respectively. The red dashed lines indicate the unit cells of the ZB structure, and the arrow in Figure 5a shows the direction of the electron beam propagation in electron diffraction. As can be seen from the image of (111) plane, when the ZB structure is rotated by 60° , the position of some Ga and N atoms within the unit cell shifts, which, according to equation (1), leads to changes in the scattering amplitude of the corresponding spots. Upon rotation by 120° , the ZB crystal structure returns to its original configuration, and the spot intensity remains unchanged. By analogy with the 6H-SiC structure⁵⁸, the 6H structure can be viewed as a ZB (111) structure with periodically spaced twins rotated by an angle of π around the [111] axis. Therefore, when the 6H structure is rotated by 60° , as shown in Figure 5b, the atomic arrangement in the twins changes symmetrically, and the intensity remains unchanged. Thus, the ZB crystal structure along the [111] direction has a three-fold rotational axis, so the $1/3$ spots clearly characterize the ZB (111) structure. The 6H crystal structure along the [0001] direction has a six-fold rotational axis, so the $1/6$ spots are unambiguously associated with the 6H polytype structure.

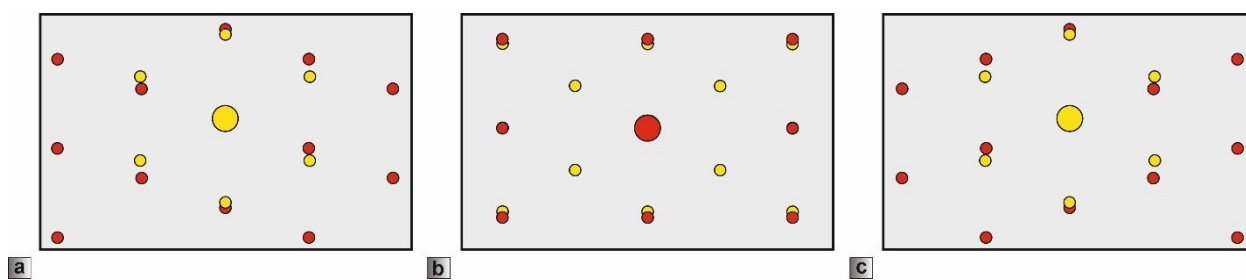


Figure 6. Simulated electron diffraction patterns of the ZB (111) and WZ (10-10) crystal structures, with red and yellow circles highlighting the fundamental spots of ZB and WZ structures, respectively. The electron beam propagates along the $[-110]$ (a), $\langle 11-2 \rangle$ (b) and $[01-1]$ (c) directions in the case of ZB structure. In the case of WZ structure, the electron beam is propagated along $\langle 11-23 \rangle$ (a), (c) and $\langle 0001 \rangle$ (b) directions.

Based on the description of the 6H structure in terms of ZB (111) structure twins, the 6H structure has the same set of fundamental spots as the ZB (111) structure⁵⁶. Consequently, the fundamental spots at azimuthal angles of 0° and 60° in Figure 1a and 1c correspond to the $\{-110\}$ and $\{11-20\}$ planes of the ZB and 6H structures, respectively. The red circles in the RHEED pattern at an azimuthal angle of 30° (see Figure 1b) and in the FFT images of individual NCs (see Figure 3b and d) highlight spots formed by the $\{11-2\}$ and $\{10-10\}$ planes of the ZB and 6H structures. Therefore, the spots highlighted with yellow circles and forming a regular hexagon belong to a different structure than ZB (111) and 6H. Among the potential planes of the ZB and WZ structures, a regular hexagon with d , similar to that of the ZB (111) and 6H structures, is formed by the fundamental spots of the WZ structure with the (10-10) plane when diffracting along the $\langle 0001 \rangle$ directions. At azimuthal angles of 0° and 60° , only the spots from ZB and 6H structures are visible, indicating that the spots from structure WZ (10-10) are either absent or masked by the spots from structures ZB and 6H. To confirm this observation, the diffraction patterns of structures WZ (10-10) and ZB (111) were simulated upon varying the azimuthal angle, given the fact that structures 6H and ZB possess the same set of fundamental spots. Figure 6a, b and c illustrate the simulation outcomes at azimuthal angles of 0 , 30 and 60° , correspondingly. The red circles highlight spots from the ZB structure (111), while the yellow circles denote those from the WZ structure (10-10). It is evident that at azimuthal angles of 0° and 60° , the spots of the WZ (10-10) structure, diffracted in the $\langle 11-23 \rangle$ directions, are masked by the spots of the ZB (111) and 6H structures. It can thus be concluded that the spots highlighted by yellow circles in both Figure 1b and Figure 3b and d correspond to the $\{0001\}$ plane of the WZ (10-10) structure. The formation of the WZ structure is consistent with the findings reported in the study by Funato et al^{56,57}, which demonstrated that the formation of the 6H structure is associated with the simultaneous formation of the ZB and WZ structures.

IVb. Formation of crystal structures

The formation of a crystal structure that differs from the stable wurtzite structure in the case of GaN nanostructures is an unusual phenomenon. Despite the different growth mechanism, somewhat similar results were obtained in the study by Jo et al⁵⁹ of the growth of nanostructures of a comparable material, ZnO, on the surface of graphene. In their study, it was demonstrated that at the initial stages of growth, ZnO nuclei exhibit a rocksalt crystal structure, which after a certain annealing time, transforms into a stable wurtzite structure with a (0001) plane. Additionally, the ZnO nanostructures are slightly misorientated with respect to each other, a phenomenon that has also been observed in GaN NCs according to RHEED patterns. This indicates the similarity of the formation processes of ZnO and GaN nanostructures on the surface of van der Waals structures. However, the key difference is that in the volume of single GaN NC different crystal phases are formed simultaneously, as evidenced by the kinetic curves of fractional spots intensity and HRTEM images. Furthermore, the formation of the most stable WZ structure with (0001) plane appears to be suppressed.

According to the literature, in the case of GaN nanostructures grown by the VLS method polytypism phenomenon is unexpected due to the relationship between the surface energy and cohesion energy of the WZ (0001) and ZB (111) phases. During the formation of the WZ (10-10) and ZB (111) phases, the inequality of surface energies for the lateral facets of the two phases changes sign, which enables the possibility of polytypism. To demonstrate the feasibility of polytypism during GaN NCs growth, a calculation was carried out using classical nucleation theory, which accurately describes polytypism during VLS growth of III-V compound nanowires⁶⁰. Let us consider the simplest model that will still allow us to describe the observed phenomenon. The formation of crystal structures within the droplet volume occurs concurrently, thereby suggesting that the nucleation within the droplet occurs in a polynuclear mode, wherein multiple nuclei are formed simultaneously. Otherwise, the formation of the ZB (111) phase on the

surface of WZ (10-10) and vice versa would be energetically unfavorable due to the different symmetries of the two phases and the necessity to introduce mismatch dislocations. This consideration limits the discussion of the formation of different phases in the volume of the droplet to the nucleation stage, on the assumption that further growth will occur with the preservation of the ratio of phases formed at the nucleation stage. Given that out of all possible polytypes, only 6H forms, it is reasonable to assume that its formation occurs exclusively at the ZB/WZ phase boundary. Therefore, the calculation was performed for the ZB (111) and WZ (10-10) phases. As will be shown later, it is sufficient to consider the specific case where ZB phase nuclei form at the triple phase line, while WZ phase nuclei form away from it. A schematic of the investigated case of ZB and WZ phase nucleation within the Ga droplet on the surface of g-SiN is shown in Figure 7.

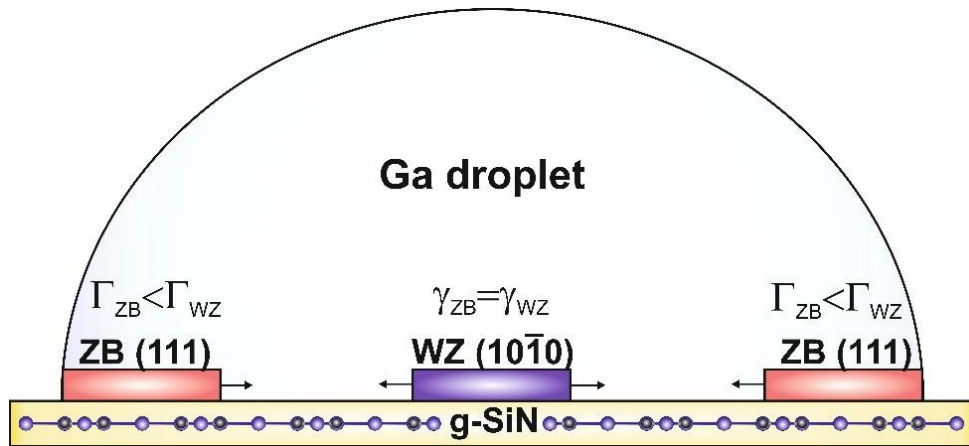


Figure 7. Schematic representation of the nucleation of ZB and WZ phases in the droplet volume on the g-SiN surface.

The nucleation barrier of the i -th phase (WZ or ZB) at the j -th position (at the three-phase boundary (TPL) or away from it) is as follows^{31,43}:

$$\Delta G_{i,j}^* = \frac{c_1^2}{4c_2} \Omega_s h \frac{\Gamma_i^2}{\Delta\mu - \psi_i} \quad (2)$$

$$\Gamma_i = \gamma_{SL}(1 - \chi) + \chi(\gamma_i - \gamma_{LV} \sin\beta) \quad (3)$$

where c_1 and c_2 are geometric constants determined by the shape of the nucleus with a height of one monolayer h . Ω_s is the volume of a Ga-N pair in the solid phase, $\Delta\mu$ is the supersaturation of the Ga-N pair in the liquid phase relative to the Ga-N pair in the solid phase, and ψ_i is the difference in cohesion energy between the i -th phase and the WZ phase. Γ_i , introduced by Glas et al.³³, is the so-called effective surface energy of the nucleus. Γ_i consists of the surface energy of the side facet completely surrounded by the liquid (γ_{SL}); the surface energy of the Ga droplet with a contact angle β (γ_{LV}); and the surface energy of the side facets of the i -th phase nucleus, which is in contact with the vapor at a fraction χ (γ_i). Let us consider nucleation of the phases at the triple phase line (TPL) and away from it. In the case of nucleation away from the TPL, $\chi = 0$, and according to equation (3), Γ_i takes the value γ_{SL} . The value of γ_{SL} for the ZB and WZ phases is assumed to be the same⁴³, and given that $\psi_{ZB} > 0$, the nucleation of the WZ phase is favorable, as $\Delta G_{ZB,C}^* > \Delta G_{WZ,C}^*$. In the case of nucleation at the TPL, $\chi > 0$, and the inequality of nucleation barriers at a given supersaturation is determined by Γ_i , which differs between the two phases only by the value of γ_i . This is clearly seen when considering the critical supersaturation $\Delta\mu_c$, above which the condition $\Delta G_{ZB,TPL}^* < \Delta G_{WZ,TPL}^*$ is fulfilled. By setting $\Delta G_{ZB,TPL}^* = \Delta G_{WZ,TPL}^*$ and solving for $\Delta\mu$, we obtain:

$$\Delta\mu > \Delta\mu_c = \frac{\psi_{ZB}}{1 - (\Gamma_{ZB}/\Gamma_{WZ})^2} \quad (4)$$

Thus, the nucleation of the ZB phase at the TPL is only possible under the condition that $\Gamma_{ZB} < \Gamma_{WZ}$, which is determined by the relation $\gamma_{ZB} < \gamma_{WZ}$. For the nucleation of the ZB and WZ phases with planes (111) and (0001), respectively, the condition $\gamma_{ZB} \geq \gamma_{WZ}$ is satisfied for any side facet of the nucleus⁶¹, thereby promoting the formation of the WZ (0001) phase. In this study, however, we observe the experimental formation of ZB and WZ phases with planes (111) and (10-10), respectively, indicating that the surface energy relationship for certain side facets, and consequently the nucleation barriers, may shift. For WZ GaN, the surface energies of non-polar planes such as (10-10) and (11-20) are well established⁶²⁻⁶⁶. However, determining the absolute

surface energy for polar planes remains a fundamental challenge, with different approaches yielding varying values of surface energy. Data on the surface energy of the ZB phase are lacking, but in the nearest-neighbor approximation, the ZB {110} and WZ {11-20} planes have the same surface energy^{43,61}, so we consider the {110} plane as the side facet of the ZB (111) phase nucleus. The side facets of the WZ (10-10) phase nucleus may include planes {0001} and {11-20}. Comparing the surface energies of the {110} and {11-20} side facets of the ZB and WZ phases, the values $\gamma_{\{110\}}$ and $\gamma_{\{11\bar{2}0\}}$ are equal, making the formation of the WZ phase more favorable. In the case of the side facets {110} and {0001}, in a variety of separate studies on the calculation of GaN surface energies⁶³⁻⁶⁵, under conditions not enriched in Ga, the values of $\gamma_{\{110\}}$ is significantly lower than $\gamma_{\{0001\}}$ (for example: $\gamma_{\{110\}} = 106 \text{ meV}/\text{\AA}^2 < \gamma_{\{0001\}} = 169.5 \text{ meV}/\text{\AA}^2$). Therefore, at least for some facets, the nucleation of the ZB phase at the TPL is possible, whereas nucleation of the WZ phase away from the TPL is clearly more favorable.

Let us perform a quantitative calculation of the probability of nucleation for the ZB (111) and WZ (10-10) phases at the TPL and away from it, respectively. Following the notations of Dubrovskii³¹, the probability of forming the ZB phase p_{ZB} can be expressed as follows:

$$p_{ZB} = \frac{P_{ZB}/P_{WZ}}{1 + P_{ZB}/P_{WZ}}$$

where P_{ZB}/P_{WZ} represents the ratio of the nucleation rates of the ZB and WZ phases, which can be written as:

$$\begin{aligned} & \frac{P_{ZB}}{P_{WZ}} \\ &= \frac{2r_c^{ZB}}{R} \exp\left(\frac{\Delta G_{WZ,C}^* - \Delta G_{ZB,TPL}^*}{k_B T}\right) \end{aligned} \quad (5)$$

where k_B is the Boltzmann constant, T is the temperature of the growth surface, R is the droplet radius, and the factor preceding the exponent r_c^{ZB} is written as: $r_c^{ZB} = \frac{c_1}{2c_2} \Omega_s \frac{\Gamma_{ZB}^2}{\Delta\mu - \psi_{ZB}}$. In equation (5), the asymptotic dependence of the phase formation rate ratio on the droplet radius is considered.

When $R \gg r_c^{ZB}$, the WZ phase predominantly forms regardless of the growth conditions, as the TPL perimeter depends linearly on R , while the area away from the TPL depends quadratically on R .

The probabilities of phase formation are directly related to the supersaturation, the determination of which, in the case of ammonia as a nitrogen source, is a challenging task. Therefore, for the calculations, we use a dimensionless chemical potential of the liquid in units of ψ_{ZB} , $f = \Delta\mu/\psi_{ZB}$ and $f_c = \Delta\mu_c/\psi_{ZB}$. As a result, the formula for the phase nucleation rate ratio of ZB and WZ is as follows:

$$\frac{P_{ZB}}{P_{WZ}} = \frac{2R_s}{R} \frac{\sqrt{1 - 1/f_c}}{f - 1} \exp\left(U_* \frac{1/f_c - 1/f}{f - 1}\right)$$

here R_s and U_* are parameters and are written in the form $R_s = \frac{c_1 \Omega_s \gamma_{SL}}{2c_2 \psi_{ZB}}$ and $U_* = \frac{c_1^2 \Omega_s h \gamma_{SL}^2}{4c_2 k_B T \psi_{ZB}}$. Let us consider the parameters used for further calculations of the nucleation probabilities of the ZB (111) and WZ (10-10) phases. The shape of the nuclei was approximated as triangular, which leads to the geometric constants $c_1 = 3$ and $c_2 = \sqrt{3}/4$, and the value $\chi = 1/3$. The droplet radius was chosen based on the average radius of the formed nanocrystals, according to atomic force microscopy data⁶⁷. The wetting angle of the Ga droplet was set to $\beta = \pi/2$. For the calculation, the value of γ_{ZB} was selected to match that of the unreconstructed, relaxed (11-20) surface. The surface energy values of the side facets of the WZ (10-10) phase, surrounded by liquid Ga, are practically unavailable; thus, γ_{SL} was adjusted to reflect the simultaneous observation of both ZB and WZ phases. The calculations were performed as a function of the dimensionless chemical potential f in the range from 0 to 15, which approximately corresponds to a range of 0 to 300 meV/pair and is typical for MBE^{33,43}. The table of parameters used for the calculation is presented below.

Table 1

c_1	c_2	Ω_s (nm^3)	h (nm)	χ	β	ψ_{ZB} (meV/pair)	γ_{LV} ($\text{meV}/\text{\AA}^2$)	γ_{ZB} ($\text{meV}/\text{\AA}^2$)
3	$\sqrt{3}/4$	0.0233	0.256	1/3	$\pi/2$	19.8	42.5	112

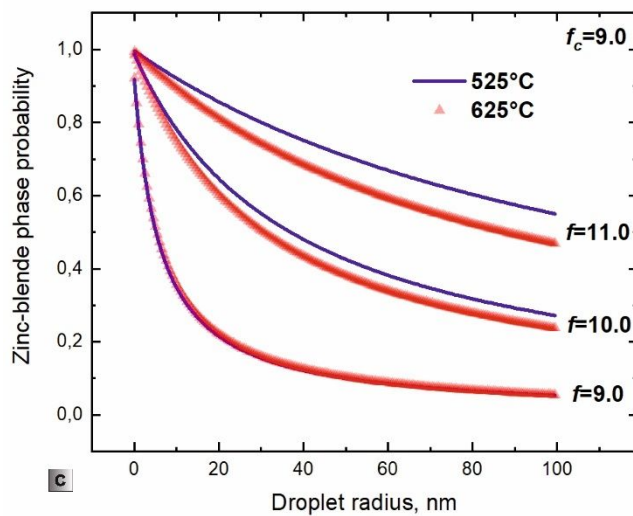
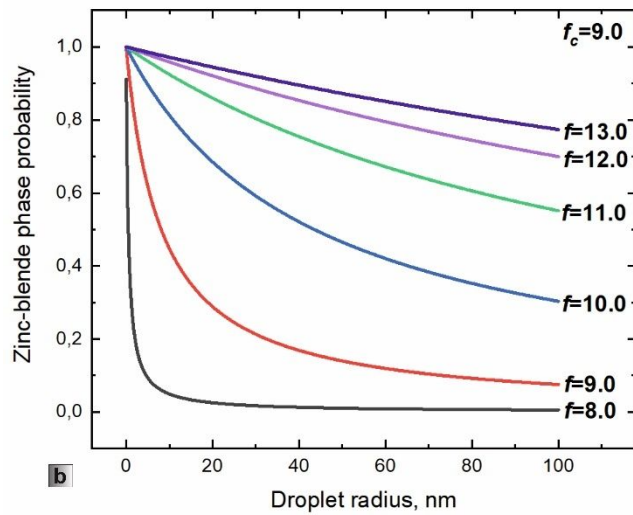
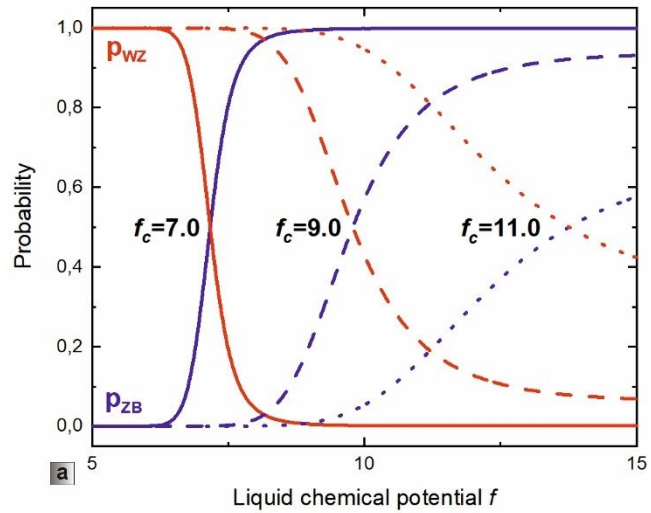


Figure 8. (a) The probability of nucleation for the ZB phase (purple curve) and the WZ phase (red curve) as a function of the dimensionless chemical potential for $f_c = 7, 9$ and 11 , corresponding to the solid, dashed and dotted lines, respectively. (b) The probability of ZB phase nucleation as a function of droplet radius for $f_c = 9$ at a dimensionless chemical potential ranging from 8 to 13 . (c) The probability of ZB phase nucleation as a function of droplet radius for $f_c = 9$ at a dimensionless chemical potential $f = 9, 10$ and 11 for temperatures of 525 °C (solid purple line) and 625 °C (red triangles).

The probabilities of ZB (111) phase nucleation at the TPL and WZ (10-10) phase nucleation away from the TPL for various f_c values are shown in Figure 8a. For given f_c values selected based on the γ_{SL} values, the probabilities of ZB and WZ phase formation in the chosen supersaturation range vary from 0 to 1 . At the lowest value, $f_c = 7$ and for $f = 10$, the ZB phase formation dominates. At the highest value, $f_c = 11$ and for $f = 10$, the WZ phase formation prevails. The γ_{SL} values in this case range from approximately 80 to 90 meV/Å², which is close to the theoretical values for the (0001) surface under Ga-rich conditions with bilayer formation^{63,64}. In the experiment, transmission diffraction is observed for both phases, making $f_c = 9$ the most suitable for describing the experimental data, where at $f = 10$ the probabilities of ZB and WZ phase formation are approximately equal, and both phases are formed. For $f_c = 9$, the probability of ZB phase nucleation as a function of droplet radius was calculated for f ranging from 8 to 13 , as shown in Figure 8b. At low f , the probability of ZB nucleation shows a sharp dependence on R , decreasing from 90% at $R = 5$ nm to almost zero at $R = 40$ nm. At high f , even at $R = 100$ nm, ZB phase formation predominates with a nucleation probability of about 80% . In consideration of the occurrence of the ZB and WZ phases within the observed temperature range, the probability of phase nucleation was calculated as a function of droplet radius at $f_c = 9$ for different f values (see Figure 8c). As demonstrated in the figure, the probability of phase formation even at temperatures 525 and 625 °C is approximately equal for droplets with radius ranging from 0 to 100 nm. This calculation is in agreement with experimental observations of the formation of different phases in the closer temperature range of 575 to 625 °C.

The dependence of the phase nucleation probability on supersaturation and droplet radius determines the possibility of controlled formation of a certain crystal phase in the NC volume. Although there is no data on the dependence of supersaturation on ammonia pressure, qualitatively, an increase in nitrogen concentration in the droplet, resulting from ammonia pressure increase, leads to a supersaturation increase and vice versa. This indicates that, at a given R , by varying the ammonia pressure within a substantial range, the formation of NCs with purely WZ or ZB crystal phase can be accomplished. The strong dependence of the phase formation probability on R at some supersaturation values suggests that a narrow droplet size distribution is necessary to avoid simultaneous formation of NCs with pure ZB and pure WZ structures.

The calculations clearly demonstrate the possibility of polytypism in GaN nanostructures, where the choice during VLS growth is reduced either to the formation of ZB (111) or WZ (10-10) phases. The question then arises as to why the formation of the WZ phase with the (0001) plane, which is more energetically favorable than the ZB (111) and WZ (10-10) phases, is not observed? One possible explanation may be found in the polarity of GaN along the [0001] direction. Unlike ZB, the lower symmetry of the WZ structure results in a non-zero dipole moment perpendicular to the (0001) plane, leading to a macroscopic electric field⁶⁸. Consequently, the surface energy of polar planes diverges, and the formation of such planes necessitates stabilization⁶⁹⁻⁷³. Stabilization involves altering the stoichiometry of the polar surface, which can be achieved through three mechanisms: surface reconstruction, surface passivation via adsorbates, and changes in the electronic structure of the surface⁶⁸. From the perspective of stabilizing the polar surface during nucleation in the volume of a Ga droplet, it follows that the only stabilization mechanism is the alteration of the electronic structure due to the transfer of a portion of the electron density from the nitrogen plane to the gallium plane. In our case, the underlying polar layer is absent, and during the formation of a nucleus one monolayer thick, the transfer of electron density is suppressed due to screening by metallic Ga. As a result, instead of the WZ (0001) phase, either

the WZ (10-10) phase or the ZB (111) phase is formed, while a 6H polytype is generated at the WZ/ZB phase boundary.

V. CONCLUSIONS

Thus, this study demonstrates the phenomenon of polytypism in GaN NCs during their growth via the VLS method on the surface of van der Waals g-SiN structures. Three phases are simultaneously formed within the NC: ZB with the (111) plane, the 6H polytype, and WZ with the (10-10) plane. Polytypism during VLS growth, particularly in nitride nanostructures, is not expected to occur due to the relationship between the surface and cohesion energies of the WZ (0001) and ZB (111) structures. In our case, the formation of the WZ structure with the polar (0001) plane is apparently suppressed due to the absence of stabilization mechanisms for the polar surface, leading to a choice during nucleation in the Ga droplet that is limited to either ZB (111) or WZ (10-10). Considering the ZB (111) and WZ (10-10) phases, calculations based on classical nucleation theory indicate the possibility of simultaneous formation of these phases within the nanocrystals over a broad range of supersaturations. Given that the 6H polytype forms at the phase boundary between ZB and WZ, the calculations suggest the potential for controlled formation of nanocrystals with either a pure ZB (111) or WZ (10-10) structure.

ACKNOWLEDGMENTS

The study was carried out within the framework of the State Assignments from the Ministry of Science and Higher Education of the Russian Federation to the Rzhanov Institute of Semiconductor Physics SB RAS (FWGW-2025-0024).

- 1 S. F. Leung, Q. Zhang, F. Xiu, D. Yu, J. C. Ho, D. Li and Z. Fan, *Journal of Physical Chemistry Letters*, 2014, **5**, 1479–1495.
- 2 G. Schmidt, C. Gould and L. W. Molenkamp, in *Physica E: Low-Dimensional Systems and Nanostructures*, 2004, vol. 25, pp. 150–159.

- 3 C. M. Cobley, J. Chen, E. Chul Cho, L. V. Wang and Y. Xia, *Chem Soc Rev*, 2011, **40**, 44–56.
- 4 M. Kulkarni, A. Mazare, E. Gongadze, Perutkova, V. Kralj-Iglic, I. Milošev, P. Schmuki, A. Iglič and M. Mozetič, *Institute of Physics Publishing*, 2015, preprint, DOI: 10.1088/0957-4484/26/6/062002.
- 5 F. Zaera, *Chem Soc Rev*, 2013, **42**, 2746–2762.
- 6 L. L. Chng, N. Erathodiyil and J. Y. Ying, *Acc Chem Res*, 2013, **46**, 1825–1837.
- 7 J. He, W. C. Cheng, Q. Wang, K. Cheng, H. Yu and Y. Chai, *Blackwell Publishing Ltd*, 2021, preprint, DOI: 10.1002/aelm.202001045.
- 8 S. K. Dubey, M. Mishra and A. Islam, *International Journal of Numerical Modelling: Electronic Networks, Devices and Fields*, DOI:10.1002/jnm.2932.
- 9 G. Li, W. Wang, W. Yang, Y. Lin, H. Wang, Z. Lin and S. Zhou, *Institute of Physics Publishing*, 2016, preprint, DOI: 10.1088/0034-4885/79/5/056501.
- 10 S. Nakamura and G. Fasol, *The Blue Laser Diode GaN Based Light Emitters and Lasers*, .
- 11 M. J. Holmes, S. Kako, K. Choi, M. Arita and Y. Arakawa, *ACS Photonics*, 2016, **3**, 543–546.
- 12 S. Deshpande, T. Frost, A. Hazari and P. Bhattacharya, *Appl Phys Lett*, DOI:10.1063/1.4897640.
- 13 J. K. Sheu, C. C. Yang, S. J. Tu, K. H. Chang, M. L. Lee, W. C. Lai and L. C. Peng, *IEEE Electron Device Letters*, 2009, **30**, 225–227.
- 14 M. Mishra, A. Gundimeda, S. Krishna, N. Aggarwal, L. Goswami, B. Gahtori, B. Bhattacharyya, S. Husale and G. Gupta, *ACS Omega*, 2018, **3**, 2304–2311.
- 15 L. Goswami, R. Pandey and G. Gupta, *Opt Mater (Amst)*, DOI:10.1016/j.optmat.2020.109820.
- 16 H. T. Chou, D. Goldhaber-Gordon, S. Schmult, M. J. Manfra, A. M. Sergent and R. J. Molnar, *Appl Phys Lett*, DOI:10.1063/1.2226454.
- 17 K. Kawasaki, D. Yamazaki, A. Kinoshita, H. Hirayama, K. Tsutsui and Y. Aoyagi, *Appl Phys Lett*, 2001, **79**, 2243–2245.
- 18 F. Bechstedt and P. Käckell, *Heterocrystalline Structures: New Types of Superlattices'?*, 1995, vol. 75.
- 19 M. Murayarna and T. Nakayama, *Chemical trend of band offsets at wurtzite/zinc-blende heterocrystalline semiconductor interfaces*, vol. 8.
- 20 Z. Ikonc, G. P. Srivastava and J. C. Inkson, *Electronic properties of twin boundaries and twinning superlattices in diamond-type and zinc-blende-type semiconductors*, vol. 48.
- 21 P. Mélinon, B. Masenelli, F. Tournus and A. Perez, *Nat Mater*, 2007, **6**, 479–490.
- 22 F. Bechstedt and A. Belabbes, 2013, preprint, DOI: 10.1088/0953-8984/25/27/273201.
- 23 K. A. Dick, C. Thelander, L. Samuelson and P. Caroff, *Nano Lett*, 2010, **10**, 3494–3499.
- 24 M. I. B. Utama, Q. Zhang, S. Jia, D. Li, J. Wang and Q. Xiong, *ACS Nano*, 2012, **6**, 2281–2288.

- 25 J. He, B. Sun, Y. Sun and C. Wang, *CrystEngComm*, 2019, **21**, 4740–4746.
- 26 S. P. Rodichkina, V. Lysenko, A. Belarouci, I. Bezverkhyy, R. Chassagnon, M. Isaiev, T. Nychyporuk and V. Y. Timoshenko, *CrystEngComm*, 2019, **21**, 4747–4752.
- 27 B. Luo, Y. Deng, Y. Wang, M. Tan, L. Cao and W. Zhu, *CrystEngComm*, 2012, **14**, 7922–7928.
- 28 S. H. Sung, N. Schnitzer, S. Novakov, I. El Baggari, X. Luo, J. Gim, N. M. Vu, Z. Li, T. H. Brintlinger, Y. Liu, W. Lu, Y. Sun, P. B. Deotare, K. Sun, L. Zhao, L. F. Kourkoutis, J. T. Heron and R. Hovden, *Nat Commun*, DOI:10.1038/s41467-021-27947-5.
- 29 X. F. Qiao, J. Bin Wu, L. Zhou, J. Qiao, W. Shi, T. Chen, X. Zhang, J. Zhang, W. Ji and P. H. Tan, *Nanoscale*, 2016, **8**, 8324–8332.
- 30 M. Kendin, M. Shaulskaya and D. Tsymbarenko, *Cryst Growth Des*, 2024, **24**, 1474–1484.
- 31 V. G. Dubrovskii, N. V. Sibirev, J. C. Harmand and F. Glas, *Phys Rev B Condens Matter Mater Phys*, DOI:10.1103/PhysRevB.78.235301.
- 32 P. Caroff, J. Bolinsson and J. Johansson, 2011, preprint, DOI: 10.1109/JSTQE.2010.2070790.
- 33 F. Glas, J. C. Harmand and G. Patriarche, *Phys Rev Lett*, DOI:10.1103/PhysRevLett.99.146101.
- 34 J. Johansson, Z. Zanolli and K. A. Dick, *Cryst Growth Des*, 2016, **16**, 371–379.
- 35 E. K. Mårtensson, S. Lehmann, K. A. Dick and J. Johansson, *Cryst Growth Des*, 2020, **20**, 5373–5379.
- 36 J. Johansson, L. S. Karlsson, K. A. Dick, J. Bolinsson, B. A. Wacaser, K. Deppert and L. Samuelson, *Cryst Growth Des*, 2009, **9**, 766–773.
- 37 H. Lu, S. Moniri, C. Reese, S. Jeon, A. Katcher, T. Hill, H. Deng and R. S. Goldman, *Appl Phys Lett*, DOI:10.1063/5.0052659.
- 38 H. Okumura A', K. Ohta, G. Feuillet, K. Balakrishnan, S. Chichibu, H. Hamaguchi, P. Hacke and S. Yoshida, *Growth and characterization of cubic GaN*, 1997, vol. 178.
- 39 B. H. Yang, K. Ploog and P. K. W B, *MBE Growth of Cubic GaN on GaAs Substrates*, 1996, vol. 194.
- 40 R. C. Powell, N. E. Lee, Y. W. Kim and J. E. Greene, *J Appl Phys*, 1993, **73**, 189–204.
- 41 R. Trejo-Hernández, Y. L. Casallas-Moreno, S. Gallardo-Hernández and M. López-López, *Appl Surf Sci*, 2023, **636**, 157667.
- 42 T. Akiyama, K. Sano, K. Nakamura and T. Ito, *Japanese Journal of Applied Physics, Part 2: Letters*, DOI:10.1143/JJAP.45.L275.
- 43 V. G. Dubrovskii, *Nanoscience and Technology Nucleation Theory and Growth of Nanostructures*, .
- 44 H. Y. Xu, Z. Liu, Y. Liang, Y. Y. Rao, X. T. Zhang and S. K. Hark, *Appl Phys Lett*, DOI:10.1063/1.3240890.
- 45 D. Tham, C. Y. Nam and J. E. Fischer, *Adv Funct Mater*, 2006, **16**, 1197–1202.

- 46 J. Arbiol, S. Estradé, J. D. Prades, A. Cirera, F. Furtmayr, C. Stark, A. Laufer, M. Stutzmann, M. Eickhoff, M. H. Gass, A. L. Bleloch, F. Peiró and J. R. Morante, *Nanotechnology*, DOI:10.1088/0957-4484/20/14/145704.
- 47 F. Furtmayr, M. Vielemeyer, M. Stutzmann, A. Laufer, B. K. Meyer and M. Eickhoff, *J Appl Phys*, DOI:10.1063/1.2980341.
- 48 T. V. Malin, V. G. Mansurov, A. M. Gilinskii, D. Y. Protasov, A. S. Kozhukhov, A. P. Vasilenko and K. S. Zhuravlev, *Optoelectronics, Instrumentation and Data Processing*, 2013, **49**, 429–433.
- 49 Y. E. Maidebura, T. V. Malin and K. S. Zhuravlev, *Semiconductors*, 2022, **56**, 340–345.
- 50 V. G. Mansurov, T. V. Malin, Y. G. Galitsyn, A. A. Shklyayev and K. S. Zhuravlev, *J Cryst Growth*, 2016, **441**, 12–17.
- 51 V. Mansurov, Y. Galitsyn, T. Malin, S. Teys, D. Milakhin and K. Zhuravlev, *Appl Surf Sci*, 2022, **571**, 151276.
- 52 J. Jo, Y. Tchoe, G. C. Yi and M. Kim, *Sci Rep*, DOI:10.1038/s41598-018-19857-2.
- 53 V. Mansurov, T. Malin, S. Teys, V. Atuchin, D. Milakhin and K. Zhuravlev, *Crystals (Basel)*, DOI:10.3390/cryst12121707.
- 54 Y. E. Maidebura, V. G. Mansurov, T. V. Malin, A. N. Smirnov, K. S. Zhuravlev and B. Pecz, *Appl Surf Sci*, DOI:10.1016/j.apsusc.2024.159595.
- 55 D. Milakhin, T. Malin, V. Mansurov, Y. Maidebura, D. Bashkatov, I. Milekhin, S. Goryainov, V. Volodin, I. Loshkarev, V. Vdovin, A. Gutakovskii, S. Ponomarev and K. Zhuravlev, *Surfaces and Interfaces*, DOI:10.1016/j.surfin.2024.104817.
- 56 M. Funato, S. Fujita and S. Fujita, *Phys Rev B Condens Matter Mater Phys*, 2001, **63**, 1–7.
- 57 M. Funato, T. Ishido, S. Fujita and S. Fujita, *Appl Phys Lett*, 2000, **76**, 330–332.
- 58 N. W. Jepps and F. Page, *POLYTYPIC TRANSFORMATIONS IN SILICON CARBIDE*, .
- 59 J. Jo, H. Yoo, S. I. Park, J. B. Park, S. Yoon, M. Kim and G. C. Yi, *Advanced Materials*, 2014, **26**, 2011–2015.
- 60 E. K. Mårtensson, S. Lehmann, K. A. Dick and J. Johansson, *Nano Lett*, 2019, **19**, 1197–1203.
- 61 N. V. Sibirev, M. A. Timofeeva, A. D. Bol'shakov, M. V. Nazarenko and V. G. Dubrovskii, *Physics of the Solid State*, 2010, **52**, 1531–1538.
- 62 H. Li, L. Geelhaar, H. Riechert and C. Draxl, *Phys Rev Lett*, DOI:10.1103/PhysRevLett.115.085503.
- 63 C. E. Dreyer, A. Janotti and C. G. Van De Walle, *Phys Rev B Condens Matter Mater Phys*, DOI:10.1103/PhysRevB.89.081305.
- 64 T. Akiyama, Y. Seta, K. Nakamura and T. Ito, *Phys Rev Mater*, DOI:10.1103/PhysRevMaterials.3.023401.
- 65 J. Zhang, Y. Zhang, K. Tse, B. Deng, H. Xu and J. Zhu, *J Appl Phys*, DOI:10.1063/1.4952395.
- 66 Razia, M. Chugh and M. Ranganathan, *Appl Surf Sci*, DOI:10.1016/j.apsusc.2021.150627.

67

68 J. Zúñiga-Pérez, V. Consonni, L. Lymperakis, X. Kong, A. Trampert, S. Fernández-Garrido, O. Brandt, H. Renevier, S. Keller, K. Hestroffer, M. R. Wagner, J. S. Reparaz, F. Akyol, S. Rajan, S. Rennesson, T. Palacios and G. Feuillet, *Appl Phys Rev*, DOI:10.1063/1.4963919.

69 A. Albar, H. A. Tahini and U. Schwingenschlögl, *NPG Asia Mater*, DOI:10.1038/AM.2017.236.

70 B. E. Gaddy, E. A. Paisley, J. P. Maria and D. L. Irving, *Phys Rev B Condens Matter Mater Phys*, DOI:10.1103/PhysRevB.90.125403.

71 N. C. Bristowe, P. B. Littlewood and E. Artacho, *Phys Rev B Condens Matter Mater Phys*, DOI:10.1103/PhysRevB.83.205405.

72 A. Kerrigan, K. Pande, D. Pingstone, S. A. Cavill, M. Gajdardziska-Josifovska, K. P. McKenna, M. Weinert and V. K. Lazarov, *Appl Surf Sci*, 2022, **596**, 153490.

73 Z. Ren, S. Qi, H. Zhou, S. Yan, M. Xu and S. Hu, *Appl Surf Sci*, 2023, **635**, 157730.